

(19)



Europäisches Patentamt  
European Patent Office  
Office européen des brevets

(11) Publication number:

**0 392 738  
A1**

(12)

**EUROPEAN PATENT APPLICATION**

(21) Application number: 90303634.1

(51) Int. Cl.<sup>5</sup>: **C25F 3/02, //B01D71/02**

(22) Date of filing: 04.04.90

(30) Priority: 14.04.89 US 338260

(43) Date of publication of application:  
17.10.90 Bulletin 90/42

(84) Designated Contracting States:  
AT BE CH DE DK ES FR GB GR IT LI LU NL SE

(71) Applicant: Sieradzki, Karl  
3703 Gardenview Road  
Baltimore, Maryland 21208(US)

Applicant: Newman, Roger C.  
2 Moss Lane  
Alderley Edge, Cheshire SK9 7HN(GB)

(72) Inventor: Sieradzki, Karl  
3703 Gardenview Road  
Baltimore, Maryland 21208(US)  
Inventor: Newman, Roger C.  
2 Moss Lane  
Alderley Edge, Cheshire SK9 7HN(GB)

(74) Representative: Burford, Anthony Frederick et al  
W.H. Beck, Greener & Co. 7 Stone Buildings  
Lincoln's Inn  
London WC2A 3SZ(GB)

(54) **Micro- and nano-porous metallic structures.**

(57) Micro- and nano-porous metallic structures are produced by contacting an alloy of at least two metals having different electrochemical activity in predetermined proportions with an electrolyte and applying an electrochemical potential to said electrolyte wherein said alloy acts as the anode until all or a portion of the more electrochemically active metal is dissolved from the alloy leaving porous metal. The resultant structure has substantially uniform and interconnected porosity in pore sizes ranging from 3 nanometers to 10 micrometers.

**EP 0 392 738 A1**

## MICRO- AND NANO-POROUS METALLIC STRUCTURES

The present invention relates to certain porous metallic structures and processes for making same. The invention particularly relates to metallic structures having very small pore sizes being of uniform and interconnected porosity. The porous metallic structures have utility, for example, as metal membranes or filters.

5 Broadly described, the porous metallic structures are produced by mixing at least two metals having significantly different electrochemical activities, according to predetermined proportions, to form a multi-metallic alloy; contacting the alloy with an electrolyte; and applying an electrochemical potential between the metal and the electrolyte wherein the alloy acts as an anode until all or a portion of the more electrochemically active metal is dissolved from the alloy leaving porous metal. The porous metal in another  
10 embodiment of the present invention is heat annealed i.e. coarsened to increase the pore size and mechanical stability of the porous metal. The structures are produced with uniform porosity in pore sizes ranging from about 3 nanometers to 10 micrometers. The porous structure can be produced in thicknesses ranging from 0.0001 to 10 mm. Depending upon the elemental composition of the membrane, the volume fraction of porosity attainable in the structures ranges from 30-80% and all of the porosity is substantially all  
15 interconnected. Membranes prepared in this way are mechanically tough, chemically inert, and heat resistant (e.g. thermally sterilizable). Such a membrane may be employed as a filter to separate particles, of size down to the molecular level, from gases and liquids.

Further objects and advantages of the present invention will be better understood by reading the following detailed description of the presently preferred exemplary embodiments of this invention in  
20 conjunction with the accompanying drawings, of which:

FIGURE 1 shows polarization curves of Ag-Au alloys in 1M perchloric acid. (a) pure Au (b)  $\text{Ag}_{0.50}\text{Au}_{0.50}$  (c)  $\text{Ag}_{0.60}\text{Au}_{0.40}$  (d)  $\text{Ag}_{0.70}\text{Au}_{0.30}$  (e)  $\text{Ag}_{0.74}\text{Au}_{0.26}$  (f)  $\text{Ag}_{0.80}\text{Au}_{0.20}$ ;

FIGURE 2 shows the electrochemical cell configuration for membrane production;

FIGURE 3 shows curves for the normalized pore size distribution for  $\text{Ag}_{0.74}\text{Au}_{0.26}$  alloy annealed 10  
25 minutes at the indicated temperatures. The pore size area, A, was normalized using the maximum pore area which developed at each of the annealing temperatures,  $A_{\text{max}}(\text{temp}^\circ\text{C})$ . These parameters are,  $A_{\text{max}}(800) = 2.45 \mu\text{m}^2$ ,  $A_{\text{max}}(700) = 0.95 \mu\text{m}^2$ ,  $A_{\text{max}}(600) = 0.55 \mu\text{m}^2$ ,  $A_{\text{max}}(500) = 0.28 \mu\text{m}^2$ , and  $A_{\text{max}}(400) = 0.24 \mu\text{m}^2$ ; and

FIGURE 4 shows curves for normalized pore aspect ratio distribution for  $\text{Ag}_{0.74}\text{Au}_{0.26}$  alloy annealed  
30 10 minutes at the indicated temperatures.

The porous metal structures are produced starting with an alloy of prescribed composition using a combination of electrochemical and thermal treatments. The starting composition of the alloy determines the volume fraction of porosity and the minimum pore size available from the particular alloy. The starting composition is determined using a scheme based upon percolation theory. The alloy is composed of  
35 elemental metals of prescribed composition with a large difference in electrochemical activity. The relative electrochemical activities of the elements are determined by the difference in the thermodynamic equilibrium metal/metal ion electrode potentials,  $\Delta E^\circ$ , as given by the electromotive force series of standard reduction potentials. By the application of an appropriate electrochemical potential in a suitable electrolyte the reactive element is selectively dissolved out while leaving the more noble element in the form of a  
40 sponge or membrane retaining the initial shape and dimensions of the sample. This allows the shape of the membrane to be pre-machined prior to the corrosion and thermal treatments as discussed below. Depending upon the system, the dissolution process may take place at various temperatures.

For a particular alloy system the "de-alloying threshold, p," is defined based upon the difference in the equilibrium metal/metal ion electron potentials of the elements in the alloy. The p defines the minimum  
45 possible concentration of the reactive element in the alloy necessary for forming the porous membrane from the remaining noble-metal and is determined from percolation theory in the following way. For elements in a binary alloy with a  $\Delta E^\circ$  greater than 0.3 Volt and less than 1.0 Volt, selective corrosion of the more reactive element can only proceed by a two-dimensional percolation process. This requires a minimum composition of the more reactive element of ca.60% atomic fraction (at%). For elements in a  
50 binary alloy with a  $\Delta E^\circ$  of 1.0 volt or greater, selective corrosion of the more reactive element proceeds by a three-dimension percolation process which allows for a minimum composition of the more reactive element of ca.30 at %. The atomic concentration of reactive element determines the volume fraction of porosity achievable in the membrane and the process of the present invention enables a volume fraction range of 30-80%. Thus, the metal to be removed comprises 30-80% of the binary alloy depending on the  $\Delta E^\circ$  of the alloy. The 80% upper limit is a result of the requirement that the remaining noble porous metal

be able to span the geometry or shape of the structure. For starting compositions greater than 80 at % of reactive element the remaining porous metal cannot maintain the initial shape of the structure and collapses. The electrolyte is chosen such that it has high solubility for the dissolved reactive metal component. The electrochemical potential is chosen to be equal to (or as close to, as allowed for by the electrolyte) the equilibrium metal/metal ion electrode potential of the more noble metal element comprising the alloy, assuming a metal ion concentration of  $\text{ca. } 10^{-6}\text{M}$ .

Metal removal by the corrosion procedure is in one embodiment of the invention, carried out to a prescribed depth as a fraction of the sample thickness, resulting in porosity to that depth.

The porous metallic structure resulting from the corrosion process, may be reinforced by two additional procedures. The resulting porous structure may be reinforced by applying i.e. lacquering a tightly adhering material impermeable to the electrolyte to selected areas of the initial alloy before contacting the alloy with the electrolyte and initiating the corrosion procedure. This prevents subsequent dissolution of the reactive metal component (e.g. silver in a silver-gold system) from the covered areas. The undissolved metal i.e. original solid, ductile alloy, is present between the dissolved regions thus providing structural support to the membrane. The solid portions of the porous structure allow for clamping and support of the structure in applications.

Another method for structurally supporting the porous metallic membrane resulting from the corrosion process, is to place a metal (e.g. copper) macroscopic mesh or other design on all or a portion of the surface of the porous metallic structure. The reinforcing material forms a composite structure providing great structural integrity.

In an embodiment of the present invention, after the corrosion procedure the resulting porous metallic structure may be subjected to heat annealing (coarsening) to increase the pore size, mechanical stability, and ductility of the structure. The unannealed structure is typically placed in a furnace for annealing.

Placing the unannealed structure directly (optionally, first rinsing the sample) into the furnace at an elevated temperature for porosity coarsening often led to sample shape distortion or warping. The warping results from the inhomogeneous temperature distribution in the structure as the structure heats up, i.e., the structure heats up from the outside in. As a result, the porous structure undergoes coarsening first near its surfaces and then in its interior. The resultant surface stresses can act to distort the sample.

Two solutions to this problem were developed and are embodiments of the present invention. The first involves the use of a rigid metal jacket cast which surrounds the structure and forces the structure to maintain its original shape. The cast is designed so that it is an adjustable stainless steel jacket which snugly surrounds the structure. A sample placed in such a jacket retained its original shape and dimensions during annealing at the desired temperature, in the furnace. The desired temperature ranges from 100-800 °C.

The other solution relies on the use of a temperature programmable furnace or similarly temperature controlled furnace. The unannealed sample is placed in the furnace at ambient temperature and the temperature is ramped (increased) linearly at a rate of less than  $10^{\circ}\text{C min}^{-1}$  until the desired temperature is attained. The desired temperature range is from 100-800 °C. This procedure is necessarily more time consuming than the procedure involving the cast where the unannealed structure is placed in the furnace at the aforementioned prescribed elevated temperature, for a prescribed time interval.

For both procedures, the time interval for continuously maintaining the prescribed temperature ranges from 2 minutes to one hour and preferably 5-30 minutes.

Both procedures can be used simultaneously to provide even less shape distortion.

For all annealing, including in-situ annealing discussed below, the mean pore size  $\langle t \rangle$  varies with time, at constant temperature, proportional to time  $t^{(0.25-0.35)}$  (preferably,  $t^{(0.30)}$ ) i.e.  $\propto t^{(1.25-0.35)}$ .

In one embodiment of the present invention, the annealed porous metallic structure may be reinforced with a metal (e.g. copper) macroscopic mesh or other design placed on the surface of the porous structure to provide greater structural support. The macroscopic mesh forms a composite like structure providing great structural integrity.

In another embodiment of the present invention, a step change in the porosity of the porous metallic structure is achieved in the following manner. Corrosion (de-alloying) is carried out to a prescribed depth which is some fraction of the sample thickness. Following this procedure, the sample is heat annealed according to the previously described procedures. The sample is removed from the furnace and once again subjected to corrosion for a prescribed period of time. A corrosion cell is employed which can be evacuated. The cell is evacuated after the membrane is placed back into the cell. The electrolyte is introduced into the cell under vacuum contacting the porous structure. This facilitates penetration of the electrolyte into the porous structure. A fine porous sponge forms at the interface of the coarse annealed porous structure and uncorroded metal. Once again the sample is placed into the furnace, but annealed at a

temperature lower than the first anneal. This allows the initial coarse structure to remain stable during the second anneal. The sample is removed and placed into the corrosion cell for further de-alloying. Again the annealing procedure is repeated at yet a lower temperature and a third layer of porosity is formed. The entire procedure may be repeated again and again thus forming a de-alloyed membrane of prescribed total thickness with step changes in porosity.

The present invention is further illustrated by the following example:

#### EXAMPLE

The processes of the present invention were employed for the production of the porous metallic structures of the invention, for example, nano- and micro-porous gold metal membranes as follows: The membranes were made from a silver-gold (Ag-Au) alloy. The  $\Delta E^\circ$  for this system was about 0.7 Volt so that the de-alloying (i.e. removal of Ag) process occurs via a two-dimensional spiral process. Silver is the more reactive element and so a minimum concentration of 60 at % Ag was required in the alloy in order to produce porous gold. A 1M perchloric acid electrolyte was employed owing to the high solubility of silver in this solution. Various concentrations of perchloric acid were tested ranging from 0.01M to 4M. Other than perchloric acid, nitric acid was also tested and found to be an appropriate electrolyte. Perchloric acid was found to be more useful in that there was a direct correlation between the quantity of Ag removed from the alloy and the total anodic charge measured as the integral of the current-time plot. The anodic current provided a direct measure of the number of Ag atoms removed every second. Since silver dissolves as  $\text{Ag}^+$ , each dissolving Ag atom is responsible for a charge of  $\text{ca } 1.6 \times 10^{-19}$  coul. The current was directly measured using the ammeter of the potentiostat. The current density is the current divided by the exposed area of the sample which is dissolving. A very high conductivity electrolyte was employed in order to lessen iR (voltage) drops down the microporous channels. The voltage drop greatly reduces the kinetics of the de-alloying process and can considerably lengthen the time required to obtain the porous solid. A 1M perchloric acid concentration was used because it represents a good balance between the high conductivity requirement and safety, i.e., perchloric acid can be an explosive mixture in concentrations between 4-10M at elevated temperatures. The employed electrochemical potential varied between 0.7 Volt and 1.4 Volt with respect to a saturated calomel electrode (SCE). The optimal voltage vis-a-vis efficiency was ca 1.1 Volt (SCE), as shown in FIGURE 1.

The Ag-Au alloys were melted in the form of 1 cm. rods or ingots under vacuum using standard procedures. The ingots were furnace cooled and then swaged so that the rod diameter was reduced by approximately 10%. Following this cold working, the alloys were placed in a furnace under vacuum and annealed at 900°C for 120 hrs. This procedure substantially removed the dendritic microstructure initially present in the as cast material, which while not necessary, provided more uniform strength of the resulting porous structure.

The behavior of Ag-Au alloys was examined in the range of compositions of 10-90 at % Ag and it was determined that the optimum composition range for gold membrane and sponge (generally, porous structure) production was 60-80 at % Ag. These results are in agreement with the previously discussed percolation model of de-alloying developed by the present inventors. FIGURE 1 shows polarization curves for selected compositions in the range examined and demonstrates the significant alteration in behavior which occurs near 60 at % Ag. For alloy compositions containing less than ca 60 at % Ag, the alloy polarization curve is similar to the polarization curve for pure gold. For alloy compositions with the Ag content greater than 60 at %, the current density rises significantly above the 0.01 mA-cm<sup>2</sup> level which is characteristic of pure gold and lower (<60 at %) silver containing alloys in the perchloric acid electrolyte. Note that the sustained plateau current (at ca 1.1V (SCE)) of the alloys does not simply scale with the silver concentration in the alloy. This is due to the fact that the selective corrosion of silver occurs by a percolation like process. The size of the porosity that develops from the silver removal controls the rate of the subsequent silver removal and is a function of the starting silver content in the alloy. The lower the initial silver content the smaller the porosity which develops in the as-corroded structure. Fine porosities will slow down the kinetics of mass transport in the electrolyte and increase iR (voltage) drops within the pores and these effects greatly reduce the kinetics of the de-alloying process. In general within the 60-80 at % Ag range, lower silver contents led to finer porosities in the as-corroded structure which slowed the kinetics of the de-alloying process. Near 60 at % Ag, the de-alloying process was extremely slow with sustained currents in the range of 0.1-1.0 mA-cm<sup>2</sup>. These current densities were not conducive for the production of thick (>100  $\mu\text{m}$ ) membranes. At the other extreme, the selective dissolution of the 80 at % Ag containing alloy resulted in gold porous structures which were extremely fragile in the as-corroded state. Scanning

electron microscopy showed that numerous cracks can develop in gold porous structures produced from alloys close to this composition.

In general, it was found that compositions close to 60 at % Ag were best for the thin (<10  $\mu\text{m}$ ) fine porosity (10 nm) membranes and that compositions close to but less than 80 at % Ag were best for the  
 5 production of thick membranes of large average porosity (about 10  $\mu\text{m}$ ).

An optimal composition was found for which a large variety of very stable porous gold membranes could be produced. This composition is  $\text{Ag}_{0.74}\text{Au}_{0.26}$  and this alloy polarization curve is shown in Figure 1. Samples of this composition could be machined prior to the corrosion procedure into any prescribed shape (e.g., cylindrical, disc, etc.,) which maintained very close tolerances during the production of the membrane.

10 Various electrode configurations were examined for mechanical stability, i.e., a corroded (at 25°C) unsupported gold sponge was very susceptible to collapse under its own weight. It was determined that supporting the Ag-Au electrode on a large mechanically stiff very flat metal sheet (3), as shown in Figure 2, made of platinum or another stable metal which serves as part of the working electrode, completely eliminated the problem of poor mechanical stability. The electrochemical cell configuration is shown in  
 15 Figure 2. Structural support of the membrane during the corrosion process was found to benefit stability.

It was found that in-situ annealing can be accomplished by performing the de-alloying at about 50-90°C and preferably 90°C. In-situ annealing increased the as-corroded ductility of the resulting porous structures. Moreover, in-situ annealing enabled the manufacture of membranes with geometries other than planar which were stable mechanically.

20 The  $\text{Ag}_{0.74}\text{Au}_{0.26}$  electrode (1) was configured for de-alloying as shown in Figure 2., in a 1.0M perchloric acid electrolyte. The  $\text{Ag}_{0.74}\text{Au}_{0.26}$  alloy was placed on the support plate which was connected as the working electrode to a potentiostat. The counterelectrode (2) material in this configuration was platinum but any suitable metal (e.g. stainless steel) or graphite would serve equally well. The electrochemical potential was set at ca 1.1 Volt (SCE) and maintained at that potential until the anodic current density dropped below  
 25 the level of 10 microamps- $\text{cm}^{-2}$ . At this current density the anode composition was >99% gold forming porous structure (4). This procedure was performed at temperatures in the range 10-90°C to form membranes (depending upon the desired characteristics of the membrane). Following the de-alloying treatment, the anode, now composed of nanoporous gold, can be transferred to a temperature controlled furnace for the annealing (coarsening) procedure.

30 Membranes of dimensions 10mm x 10mm x 1.5mm thick were fabricated from an ingot of  $\text{Ag}_{0.74}\text{Au}_{0.26}$  alloy using the ambient temperature selective corrosion process described above. Subsequent samples were encapsulated in a cast stainless steel jacket and inserted into the annealing furnace at a prescribed temperature for a time of 10 minutes. The resultant membrane characteristics are listed in the table below.

35

40

45

50

55

TABLE:

Characteristics of membranes manufactured from a $\text{Ag}_{0.74}\text{Au}_{0.26}$ alloy.				
The Table below lists the resulting characteristics of the membranes obtained. The abbreviations in the table refer to the following: E, the elastic Young's modulus of the membrane; S the fracture stress; $\langle l \rangle$ the average pore size of the membrane; and A, the average pore area;				
Temp(°C)	A( $\mu\text{m}^2$ )	$\langle l \rangle$ ( $\mu\text{m}$ )	E(MPa)	S(MPa)
25 (room temp.)	$6 \times 10^{-6}$	0.002*	**	**
100	$2.5 \times 10^{-5}$	0.005	240	0.55
200	0.0004	0.02	190	0.65
300	0.002	0.04	160	0.80
400	0.01	0.10	100	1.10
500	0.02	0.14	100	1.30
600	0.07	0.26	97	1.45
700	0.20	0.44	55	1.50
800	1.53	1.25	47	3.00

\*Estimated by linear extrapolation

\*\*Not determined

The void size distributions for the samples annealed at 800, 700, 600, 500 and 400°C are shown in Figure 3, and the aspect ratio distributions for these samples are shown in Figure 4. The distributions almost superpose on one another indicating the self-similar nature of the coarsening process operative during annealing. Thus the uniformity of the pore size is assured within the range of temperatures examined.

The mechanical properties of the membranes are listed in the table above. In general the smaller pore size membranes have a larger Young's modulus and a smaller fracture stress than the larger pore size membranes. It was also determined that the toughness or ductility of the membrane was a function of the ratio of the membrane thickness, W, to the average pore size. For membranes with  $W/\langle l \rangle$  less than 10,000 the membranes were tough and ductile, while for membranes with  $W/\langle l \rangle$  significantly greater than 10,000 the membranes were brittle. It was found that the very small pore size membranes can be toughened or ductilized by decreasing the thickness of the membranes such that the value of  $W/\langle l \rangle$  is less than 10,000.

While only a few exemplary embodiments of the present invention have been described in detail, those skilled in the art will recognize that the invention is not restricted to said embodiments but is defined in the following claims.

#### Claims

1. A process for producing micro- and nano-porous metallic structures comprising contacting an alloy of at least two metals having different electrochemical activity in predetermined proportions with an electrolyte and applying an electrochemical potential to said alloy wherein said alloy acts as the anode until all or a portion of the more electrochemically active metal is dissolved from the alloy leaving porous metal.

2. A process as claimed in Claim 1, wherein said alloy is a binary alloy containing 60-80% of the less noble metal and 40-20% of the more noble metal.

3. A process as claimed in Claim 1 or Claim 2, wherein said alloy is a binary alloy of silver or gold.

4. A process as claimed in Claim 3, wherein silver forms 74% and gold forms 26% of said binary alloy.

5. A process as claimed in Claim 3 or Claim 4, wherein said electrolyte is perchloric acid or nitric acid.

6. A process as claimed in any one of the preceding claims, wherein said porous metal is heated for a predetermined period of time to anneal said porous metal.

7. A process as claimed in Claim 6, wherein the temperature of said electrolyte is maintained at 50-

90 °C, for a predetermined period of time, for in-situ annealing.

8. A process as claimed in any one of the preceding claims, wherein selected areas of said alloy are masked before contacting with said electrolyte, to prevent or reduce subsequent dissolution of the less noble metal from said covered areas, the undissolved areas providing support to the resulting porous metal.

5 9. A process as claimed in any one of the preceding claims, wherein the less noble metal is dissolved from only the surface of said alloy to a predetermined depth.

10. A process as claimed in Claim 9, wherein:

(a) said porous metal is heated for a predetermined period of time, to anneal said porous metal;

(b) the annealed porous metal is placed into a corrosion cell and said cell evacuated;

10 (c) electrolyte is introduced into said evacuated cell, contacting the porous metal;

(d) an electrochemical potential is applied to said alloy wherein said metal acts as an anode until additional less noble metal is dissolved from beneath the porous metal leaving fine porous metal at the interface of the annealed porous structure and undissolved metal;

(e) said porous metal of step (d) is heated at a lower temperature than annealing step (a) for a 15 predetermined period of time, to anneal said porous metal; and

(f) optionally, repeating steps (a)-(e) for a predetermined ("n") number of cycles to produce a porous metal of prescribed thickness with "n" number of step changes in porosity with depth from the surface of said porous metal.

11. A porous metal structure obtainable by a process as claimed in Claim 1 and having substantially 20 uniform and interconnected porosity, with pore sizes ranging from 3 nanometers to 10 micrometers.

12. A porous metal structure as claimed in Claim 11 comprising a binary alloy substantially formed of gold with less than 1% silver.

13. A porous metal structure as claimed in Claim 11 or Claim 12, wherein said structure has a thickness ranging from 0.0001 to 10mm.

25 14. A porous metal structure as claimed in any one of Claims 11 to 13, wherein the degree of porosity changes with depth in a step fashion from the surface of said structure.

30

35

40

45

50

55

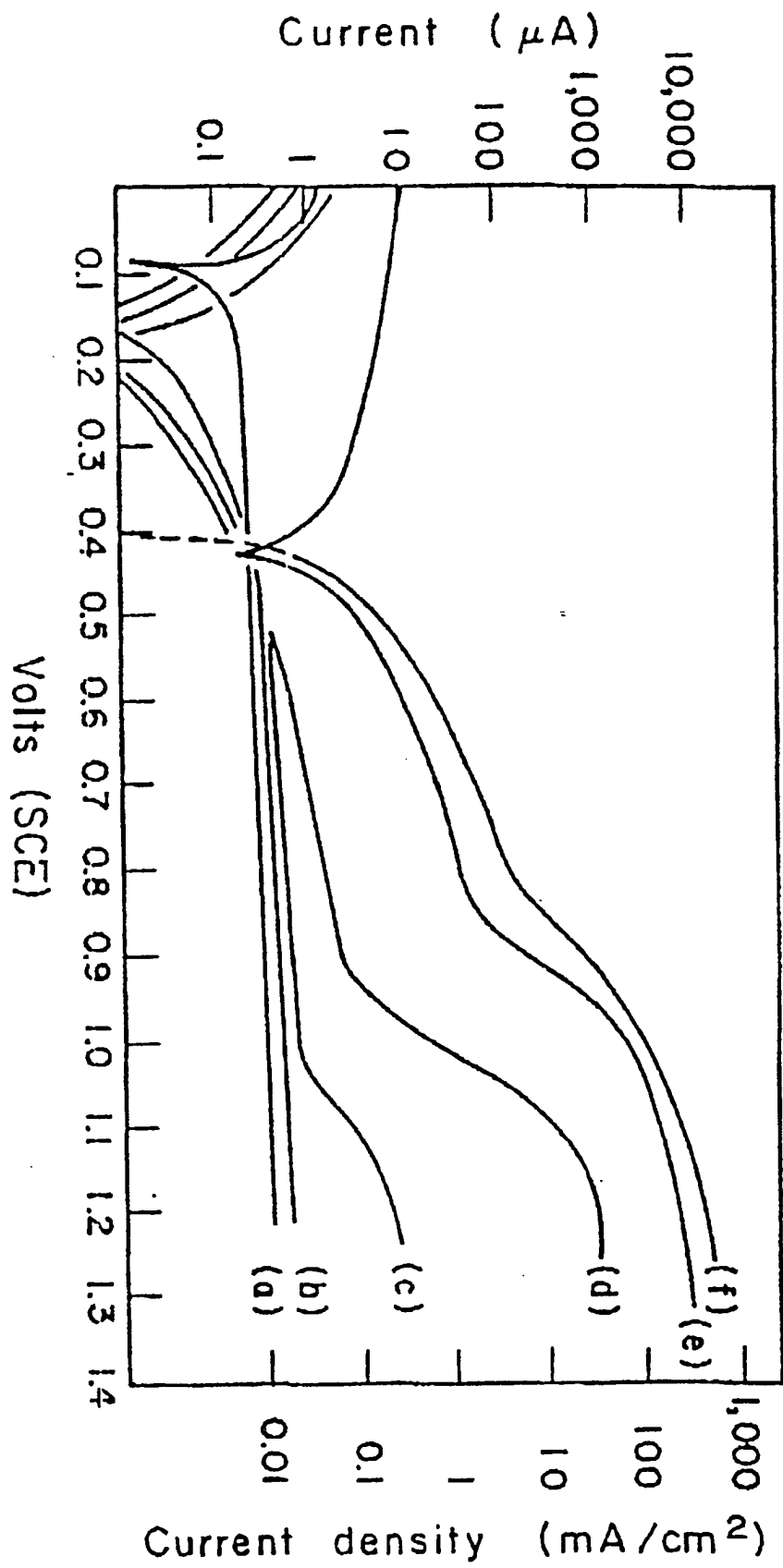


Figure 1.



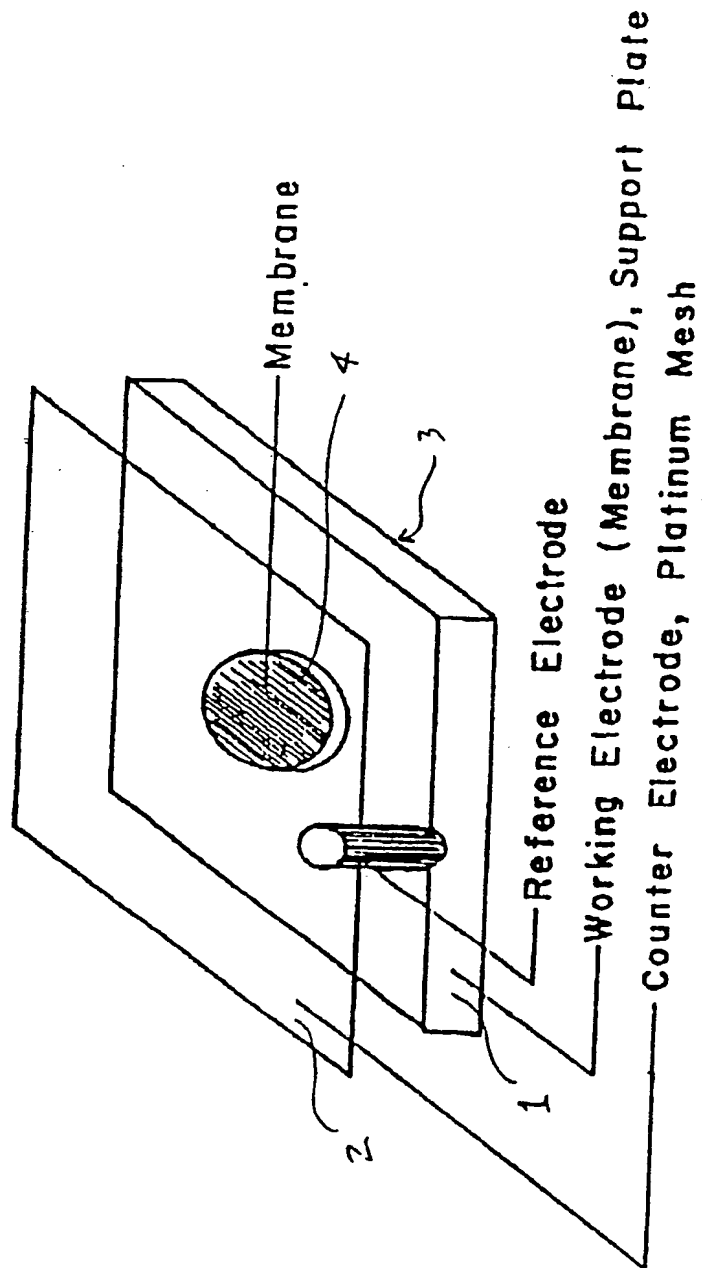


Figure 2.

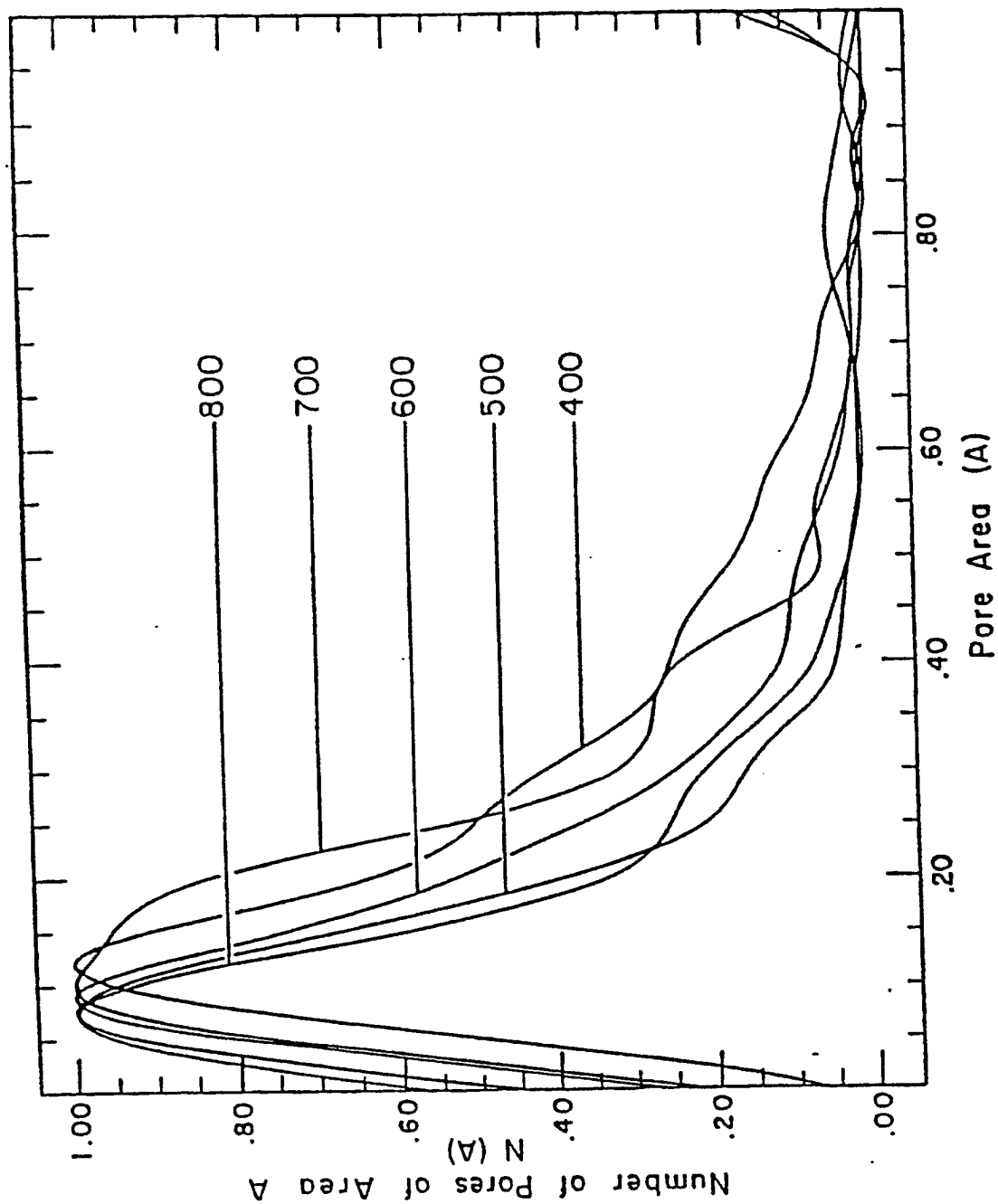


Figure 3.

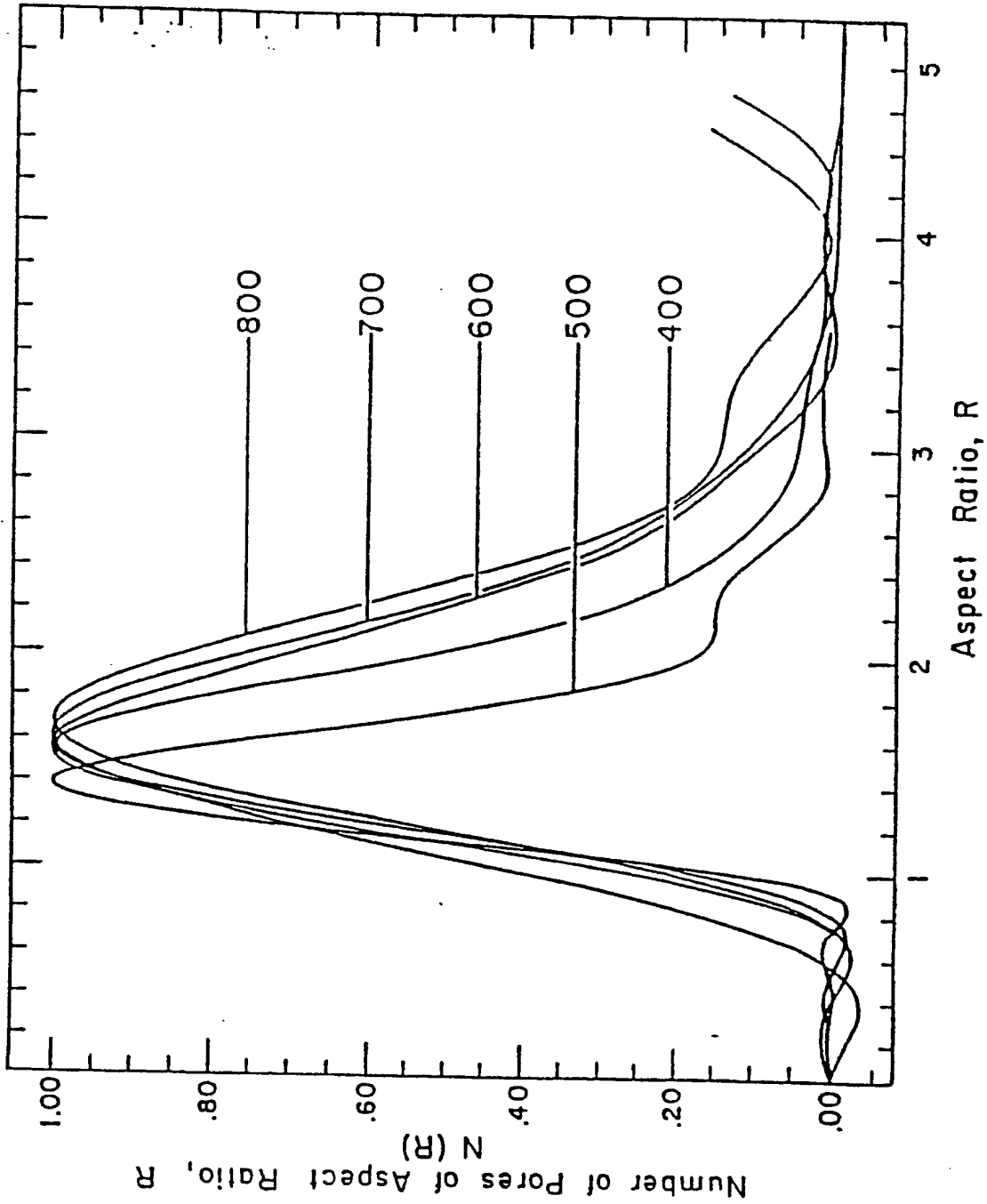


Figure 4.



European Patent  
Office

# EUROPEAN SEARCH REPORT

Application Number

EP 90 30 3634

DOCUMENTS CONSIDERED TO BE RELEVANT			
Category	Citation of document with indication, where appropriate, of relevant passages	Relevant to claim	CLASSIFICATION OF THE APPLICATION (Int. Cl.5)
X	US-A-3 533 863 (LEE) * Column 2, lines 1-19; column 3, lines 25-65; column 4, lines 40-46; claim 5; example 2 * -----	1,3,5,9 ,11,13	C 25 F 3/02 // B 01 D 71/02
			TECHNICAL FIELDS SEARCHED (Int. Cl.5)
			C 25 F 3/00 C 25 F 3/02 C 25 F 3/14 B 01 D 71/02
The present search report has been drawn up for all claims			
Place of search THE HAGUE		Date of completion of the search 02-08-1990	Examiner VAN LEEUWEN R.H.
<b>CATEGORY OF CITED DOCUMENTS</b> X : particularly relevant if taken alone Y : particularly relevant if combined with another document of the same category A : technological background O : non-written disclosure P : intermediate document T : theory or principle underlying the invention E : earlier patent document, but published on, or after the filing date D : document cited in the application L : document cited for other reasons ..... & : member of the same patent family, corresponding document			

## Evolution of nanoporosity in dealloying

Jonah Eriebacher<sup>\*†</sup>, Michael J. Aziz<sup>\*</sup>, Alain Karma<sup>‡</sup>, Nikolay Dimitrov<sup>§</sup> & Karl Sieradzki<sup>§</sup>

<sup>\*</sup> Division of Engineering and Applied Sciences, Harvard University, 9 Oxford Street, Cambridge, Massachusetts 02138, USA

<sup>†</sup> Department of Physics and Center for Interdisciplinary Research on Complex Systems, Northeastern University, 360 Huntington Avenue, Boston, Massachusetts 02115, USA

<sup>§</sup> Department of Mechanical and Aerospace Engineering and Center for Solid State Sciences, Arizona State University, Tempe, Arizona 85287-6106, USA

Dealloying is a common corrosion process during which an alloy is 'parted' by the selective dissolution of the most electrochemically active of its elements. This process results in the formation of a nanoporous sponge composed almost entirely of the more noble alloy constituents<sup>1</sup>. Although considerable attention has been devoted to the morphological aspects of the dealloying process, its underlying physical mechanism has remained unclear<sup>2</sup>. Here we propose a continuum model that is fully consistent with experiments and theoretical simulations of alloy dissolution, and demonstrate that nanoporosity in metals is due to an intrinsic dynamical pattern formation process. That is, pores form because the more noble atoms are chemically driven to aggregate into two-dimensional clusters by a phase separation process (spinodal decomposition) at the solid-electrolyte interface, and the surface area continuously increases owing to etching. Together, these processes evolve porosity with a characteristic length scale predicted by our continuum model. We expect that chemically tailored nanoporous gold made by dealloying Ag-Au

should be suitable for sensor applications, particularly in a biomaterials context.

Selective dissolution has a long history<sup>3</sup>. For example, the chemical treatment known as depletion gilding selectively dissolves a non-gold element near the surface of a less-expensive alloy such as Au-Cu, leaving behind a surface of pure gold. Early Andean goldsmiths used this technique to enhance the surfaces of their artefacts<sup>4</sup>. In this century, selective dissolution has been primarily examined in the context of corrosion. It is observed in technologically important alloy systems, notably brasses, stainless steels, and Cu-Al alloys<sup>1,5,6</sup>. The mechanical properties of a porous overlayer are very different from the bulk alloy on which it sits, leading to brittle crack propagation, stress corrosion cracking, and other undesirable materials failure<sup>7</sup>. Figure 1 shows the prototypical dealloyed microstructure, that of nanoporous gold. Early notions considered porosity as a hidden microstructure revealed by etching, but diffraction experiments showed that no pre-existing length scale exists before acid attack on single-phase alloys<sup>8,9</sup>. Later ideas considered the influence of percolating clusters within the solid solution of the alloy, but models failed to yield behaviour consistent with experiment<sup>10,11</sup>.

The following argument illustrates the fundamental obstacle to understanding porosity formation during dealloying: consider a silver-gold alloy in an electrolyte under conditions where silver dissolves and gold is inert. Initially, silver will be dissolved from surface sites such as terraces or steps. Gold atoms should accumulate on the surface and locally block further dissolution. For an alloy containing 10% gold, it might be expected that dissolution would stop or be significantly retarded after about 10 monolayers of the alloy have been dissolved.

A complete model of selective dissolution needs to be multi-scale, involving the kinetics of dissolution, surface diffusion, and mass transport through the bulk of both alloy and electrolyte. Because

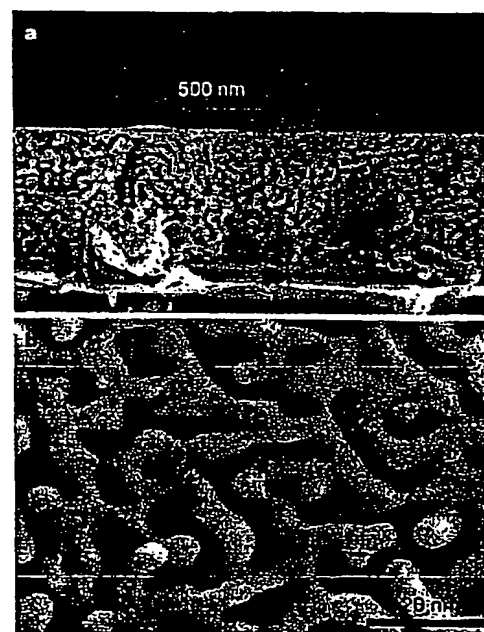


**Figure 1** Scanning electron micrographs of nanoporous gold made by selective dissolution of silver from Ag-Au alloys immersed in nitric acid under free corrosion conditions. **a**, Cross-section of dealloyed Au<sub>32</sub>Ag<sub>68</sub> (atom%) thin film. **b**, Plan view of dealloyed Au<sub>26</sub>Ag<sub>74</sub> (atom%). The porosity is open, and the ligament spacings shown in **b** are of the order of 10 nm; spacings as small as 5 nm have been observed. Measurements of the surface area of nanoporous gold are of the order of order 2 m<sup>2</sup> g<sup>-1</sup> (refs 24, 25), comparable to commercial supported catalysts.

mass transport through the bulk of the growing phase (the electrolyte) is always a stabilizing influence<sup>11</sup>, and because mass transport through the bulk of the dissolving phase appears too slow to be significant, we hypothesized that the morphology-determining physical process is confined to the interface region between the alloy and the electrolyte. To test this, we developed a kinetic Monte Carlo model to simulate Ag-Au dealloying, including only diffusion of silver and gold and dissolution of silver<sup>12</sup>. We found that this model was able to reproduce all relevant experimental trends characteristic of dealloying, both morphological and kinetic.

Figure 2 shows a simulated porous structure with ligament widths of 2–5 nm. Our simulations were successful in modelling the nanoporous morphology, and also in modelling the dynamic behaviour of the dissolution current versus overpotential. It is a well characterized feature of alloy dissolution that as the overpotential is increased (usually at rates of the order of a few millivolts per second), the dissolution current of ions from the alloy stays at a low level until a bulk-composition-dependent critical potential ( $V_c$ ) is reached, at which point this current rises rapidly<sup>14</sup>. Figure 3 shows simulated and experimental polarization curves for different alloy compositions. There is clear observation of a composition-dependent  $V_c$ . To our knowledge, this is the first simulation model to produce such behaviour, suggesting that we have found a minimum set of physical processes to include in any model for

alloy dissolution.

The simulations reveal the following qualitative picture of porosity formation. The process starts with the dissolution of a single silver atom on a flat alloy surface of close-packed (111) orientation, leaving behind a terrace vacancy. The atoms coordinating this vacancy have fewer lateral near-neighbours than other silver atoms in the terrace, and are thus more susceptible to dissolution. As a result, the entire terrace is 'stripped', leaving behind gold atoms with no lateral coordination ('adatoms'). Before the next layer is attacked, these gold adatoms diffuse about and start to agglomerate into islands. As a result, rather than a uniform diffuse layer of gold spread over the surface, the surface is comprised of two distinct kinds of regions—pure gold clusters that locally passivate the surface, and patches of un-dealloyed material exposed to electrolyte. When silver atoms in these patches dissolve, more gold adatoms are released onto the surface. These adatoms diffuse to the gold clusters left over from dissolution of previous layers, continuing to leave un-dealloyed material exposed to electrolyte. In the early stages, these gold clusters are mounds that are gold-rich at their peaks and that have alloy composition at their bases. These mounds get undercut, increasing the surface area that gold must cover to bring about passivation. Ultimately, this leads to pit formation and porosity.

Central to this description is the coalescence of gold adatoms into stable clusters. The spacing between these 'islands' in the initial stages of dissolution is close to the spacing between ligaments in the final porous structure. The physical reason for this coalescence can be understood by considering the gold adatoms to be one component of a two-component solution of gold and 'electrolyte' confined to the monolayer-thick interfacial layer sitting on top of un-dealloyed material. We modelled the thermodynamics of the interfacial layer as a regular solution<sup>15</sup>, and found the solubility of gold in electrolyte within the interfacial layer to be of the order of  $10^{-7}$  per site (see Methods). This solubility may be interpreted as the 'equilibrium concentration of gold adatoms' on the surface of the alloy—in the absence of etching, it represents a dynamic equilibrium of adatoms resulting from their two-dimensional evaporation from step edges onto terraces and their subsequent recondensation.

In contrast to the equilibrium condition, rapidly stripping a terrace of silver atoms leaves gold adatoms with a local site occupancy fraction equal to that in the bulk, typically 10–40%—far above their equilibrated concentration of  $10^{-7}$  per site. Thus, there is an extremely strong driving force for gold adatoms to condense onto nearby gold-rich clusters. In fact, regions of surface with high enough supersaturation of gold adatoms sit 'within the spinodal', a special segment of the curve representing free energy  $f$  of a spatially uniform layer versus gold concentration  $C$  for which  $\partial^2 f / \partial C^2 < 0$ . Within the spinodal, composition fluctuations of infinitesimal amplitude lead to a lower overall free energy for the



**Figure 2** Simulated nanoporous gold. The simulation model was as follows: a bond-breaking model was used for diffusion; atoms with  $N$  near neighbours diffused with rate  $k_N = \nu_0 \exp(-N\epsilon/k_B T)$ , where  $\epsilon$  is a bond energy and  $\nu_0 = 10^{13} \text{ s}^{-1}$ . Dissolution rates were consistent with the Butler-Volmer (BV) equation in the high-driving-force Tafel regime; the dissolution rate  $k_{Au}$  for a silver atom with  $N$  near neighbours was written as  $k_{Au} = \nu_E \exp[-(N\epsilon - \phi)/k_B T]$ , where  $\nu_E = 10^4 \text{ s}^{-1}$  is an attempt frequency determined by the exchange-current density in the BV equation and  $\phi$  is the overpotential. For the figure,  $\phi = 1.75 \text{ eV}$ ,  $e/k_B T = 5.51$ .

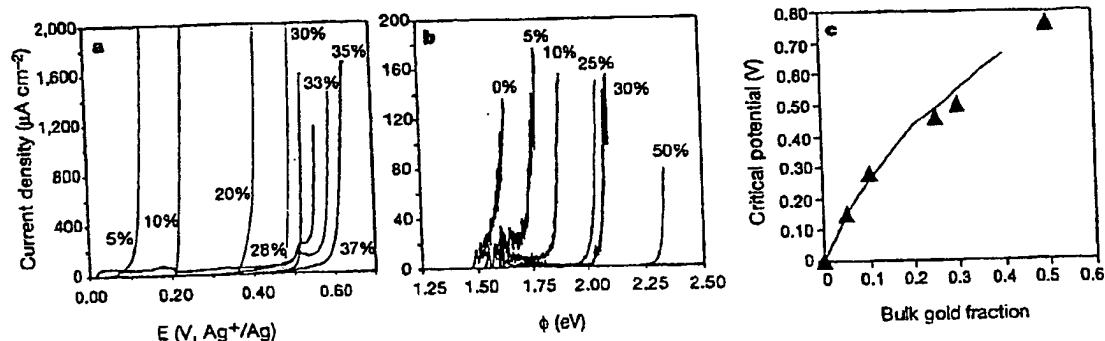


**Figure 3** Comparison of experimental and simulated current-potential behaviour. **a**, Current-potential behaviour for varying Ag-Au alloy compositions (atom% Au) dealloyed in 0.1 M  $\text{HClO}_4$  + 0.1 M  $\text{Ag}^+$  (reference electrode 0.1 M  $\text{Ag}^+/\text{Ag}$ ). **b**, Simulated

current-potential behaviour of Ag-Au alloys. **c**, Comparison of experimental (line) and simulated (triangles) critical potentials; the zero of overpotential has been set equal to the onset of dissolution of pure silver both in simulation and in experiment.

system, and involve atomic diffusion against concentration gradients (the 'uphill diffusion' process through which gold condenses onto nearby clusters), that is, the system is inherently unstable and will spontaneously phase-separate. But fluctuations of long length scale grow slowly due to the required diffusion times, and short-length-scale fluctuations create much energetically unfavourable incipient interface between the phases, inhibiting their growth. Hence, phase separation is manifested most rapidly at an intermediate length scale that roughly corresponds to the spacing between the observed gold-rich clusters. This effect is known as spinodal decomposition<sup>16,17</sup>. As porosity forms, the decomposition is occurring on a non-flat, non-uniform surface with continuously increasing surface area.

In our model, the motion of the alloy–electrolyte interface is fully described mathematically by the flux of diffusing adatoms  $J_s$ , the velocity of the interface normal to itself  $v_n$ , and the concentration accumulation rate  $\partial C/\partial t$ , all of which are interrelated and vary with position along the curve of the interface (for detailed derivations, see Methods). For  $J_s$ , we used a model for diffusion during spinodal decomposition known as the Cahn–Hilliard equation<sup>17</sup>. The normal velocity depends on  $C$  and also on the local curvature  $\kappa$  through capillary effects<sup>11</sup>. The time evolution of  $C$  is uniquely determined by the local mass-conservation condition

$$\partial C/\partial t = v_n C_0 - v_n \kappa C - \nabla \cdot J_s \quad (1)$$

where  $C_0$  is the bulk gold concentration. This condition is analogous to the local conservation of heat or solute appearing in boundary-layer models of solidification<sup>18</sup>, with two important differences: (1) the interfacial layer thickness is constant along the interface, and is microscopic, rather than being a spatially varying macroscopic diffusion length, and (2) the surface aggregation process inherent in the Cahn–Hilliard form for  $J_s$  is essential for porosity formation. Simple ('downhill') surface diffusion ( $J_s = -D_s \nabla C$ ) yields an

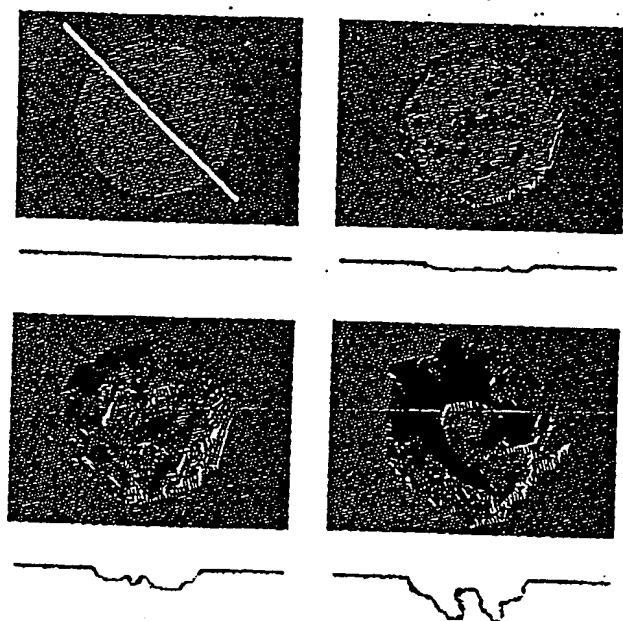


**Figure 4** Simulated evolution of an artificial pit in  $\text{Au}_{10}\text{Ag}_{90}$  (atom%),  $\phi = 1.8$  eV. Cross-sections along the  $(111)$  plane defined by the yellow line in **a** are shown below each plan view. **a**, The initial condition is a surface fully passivated with gold except within a circular region (the 'artificial pit'). **b**, After 1 s, the pit has penetrated a few monolayers into the bulk. We note how there are fewer gold clusters near the side wall than at the centre of the pit. **c**, After 10 s, a gold cluster has nucleated in the centre of the pit. **d**, At 100 s, the pit has split into multiple pits; each will continue to propagate into the bulk to form a porous structure like that in Fig. 2.

initially unstable interface that passivates quickly, before well-formed pores have a chance to develop. Cahn–Hilliard diffusion also dominates capillarity-driven surface diffusion—the effect usually incorporated into interface evolution equations<sup>19</sup>.

We performed numerical integration of equation (1) using a relative arc-length parametrization scheme<sup>20,21</sup>, and parameters that matched those used in the kinetic Monte Carlo simulations. We observed, as expected, the evolution of gold clusters separated by a characteristic spacing  $\lambda$ . An analytic expression for  $\lambda$  can be found by a time-dependent linear stability analysis of equation (1) that takes into account the slow increase of gold concentration into the interfacial layer as the instability develops. This effect needs to be included because the spatial period with the largest amplification rate depends sensitively on the gold concentration. Specifically, this spatial period decreases sharply as the concentration increases past a threshold concentration for instability that corresponds to the spinodal point  $\partial^2 f/\partial C^2 = 0$ , and the interface is stable for concentrations below this threshold. We find a maximally unstable spatial period that scales as  $\lambda \propto (D_s/V_0)^{1/6}$ , where  $V_0$  is the velocity of a flat alloy surface with no gold accumulated upon it. This prediction is in qualitative agreement with both kinetic Monte Carlo simulations and experiments, both of which show that the characteristic length scale of porosity decreases with increasing driving force. A more elaborate analysis incorporating nonlinear effects, however, remains needed for a detailed quantitative comparison.

There is an analogy between this result, applicable to etching, and two-dimensional island nucleation during submonolayer vapour phase deposition. Namely, in the early stages of etching, the dissolution process is analogous to deposition of gold; in both processes, adatoms are added to the surface where they are free to agglomerate into islands. The case of vapour phase deposition has been studied using rate equations that describe an aggregation process where adatoms stick together irreversibly. In these studies it is a well-known result that the island spacing scales as  $(D_s/F)^{1/2}$ , where the deposition rate  $F$  is the direct analogue of the surface velocity in etching, and the exponent  $\mu$  depends on details of the aggregation process (see ref. 22 and references therein). That these results are limited to irreversible aggregation during deposition and our analysis is for reversible aggregation during etching suggests the existence of universal scaling laws for aggregation that do not depend on reversibility or the lack thereof in these two opposite processes.

Our kinetic Monte Carlo simulation elucidates the later stages of morphological evolution, and the mechanism by which three-dimensional porosity evolves. We highlight the features of this process by showing in Fig. 4 a simulation of an artificial pit in an otherwise fully passivated surface. When the pit reaches sufficient depth, its surface area has increased sufficiently that a new gold cluster nucleates. When this happens, the pore splits into multiple new pits, each with a smaller surface area than its parent. These 'child' pits continue to penetrate into the bulk, increasing their surface area, nucleating new clusters, spawning new pits, and so on, until a full, three-dimensional porous structure evolves, such as those illustrated in Figs 1 and 2. □

## Methods

In a regular solution, the enthalpy of mixing depends on the bond energies and the entropy of mixing is ideal. The free energy of a regular solution  $f(C, T)$  is written  $f = \alpha c(1-c) + k_B T [c \ln c + (1-c) \ln(1-c)]$ , where  $c$  is the mole fraction of gold ( $c = C/\Omega$ ), where  $\Omega$  is atomic volume),  $\alpha = 6[E_{\text{Au-electrolyte}} - (1/2)(E_{\text{Au-Au}} + E_{\text{electrolyte-electrolyte}})]$ , where  $E_{\text{Au-Au}}$  are the respective interaction energies between Au and electrolyte, the prefactor 6 is the lateral coordination in the two-dimensional hexagonal lattice of the interfacial layer,  $k_B$  is Boltzmann's constant and  $T$  is absolute temperature. For our simulation conditions, realistic timescales and length scales were obtained from the parameters  $E_{\text{Au-Au}} = -0.245$  eV,  $E_{\text{Au-electrolyte}} = -0.245$  eV, the simulation bond energy as described in Fig. 2),  $T = 600$  K,  $E_{\text{electrolyte-electrolyte}} = E_{\text{Au-electrolyte}} = 0.0$  eV. With these parameters,  $\alpha = 0.855$  eV. The free energy has the familiar double-well form<sup>23</sup> and a minimum at  $c \approx 10^{-2}$  per site, representing the solubility of gold in electrolyte (and vice versa).

The Cahn–Hilliard diffusion equation is  $J_s = -M(C)\nabla^2 f/\nabla C + 2M(C)\nabla^3 C$ .

Here,  $453M(C)$  is a mobility,  $w$  is the so-called gradient energy coefficient, and the gradients are taken with respect to arc length. The first term on the right-hand side describes the chemical effect leading to phase separation within the spinodal; the second term describes the effect that damps short-wavelength fluctuations. The mobility is proportional to the surface diffusivity  $D_s$  and is given by  $M(C) = (D_s/k_B T) c(1-c)$ . The mobility is peaked for  $c = 0.5$ , and is zero for  $c = 0$  and  $c = 1$  (atoms do not diffuse in pure phases because there are no vacancies in our model). The normal velocity is given by  $v_n(C) = V(C)[1 - (\gamma\Omega/k_B T)\epsilon]$ , where  $\gamma$  is the surface free energy and  $V(C)$  is called the interface response function, equal to the velocity of a flat surface covered with a concentration  $C$  of gold. We find in both simulation and experiment that the interface response is fitted well by the functional form  $V(C) = V_0(\phi)\exp(-C/C^*)$ , where  $\phi$  is the overpotential and  $C^*$  is a constant. Experimentally, the gold accumulation can be inferred by integrating the dissolution current versus time at fixed overpotential; it is necessary to use an overpotential that is low enough to ensure that the surface remains planar (that is, porosity does not form) and also to catch the short initial transient rise in current as silver atoms are pulled from the first few monolayers. This particular form for the interface response function is quite curious. Naively, one might expect that the local interface velocity would be proportional to the local concentration of silver exposed to the electrolyte, that is,  $V(C) \propto (1-c)$ . However, the decaying exponential form suggests that there is an evolving distribution of holes opening and closing within the interfacial region, controlling the accumulation rate.

Physically, the mass conservation condition (equation (1)) is the statement that the total number  $Cb\Delta s$  of gold atoms in a length  $\Delta s$  of interface with lateral width  $b$  can change as a result of three distinct effects that correspond to the three terms on the right-hand-side of equation (1): the accumulation of gold atoms into the interfacial layer from the solid being dissolved; the local stretching of the interface ( $\partial\Delta s/\partial t = v_n \Delta s$ ), which can either increase or decrease  $C$  depending on whether the solid is concave ( $\kappa > 0$ ) or convex ( $\kappa < 0$ ); and the motion of atoms along the interface driven by the surface diffusion flux  $J_s$ .

Received 14 November 2000; accepted 10 January 2001.

- Pickering, H. W. Characteristic features of alloy polarization curves. *Corros. Sci.* **23**, 1107–1120 (1983).
- Fory, A. J. Corrosion micromorphology of noble metal alloys and depletion pitting. *Nature* **282**, 597–598 (1979).
- Masing, G. Zur Theorie der Resistenzgrenzen in Mischkristallen. *Z. Anorg. Allg. Chem.* **118**, 293–308 (1921).
- Lechtman, H. Pre-Columbian surface metallurgy. *Sci. Am.* **250**, 56–63 (1984).
- Williams, D. E., Newman, R. C., Song, Q. & Kelly, R. G. Passivity breakdown and pitting corrosion of binary alloys. *Nature* **350**, 216–219 (1991).
- Newman, R. C. & Sieradzki, K. Metallic Corrosion. *Science* **263**, 1708–1709 (1994).
- Li, R. & Sieradzki, K. Ductile-brittle transition in random porous Au. *Phys. Rev. Lett.* **68**, 1168–1171 (1992).
- Corcoran, S. in *Critical Factors in Localized Corrosion III* (eds Kelly, R. G., Frankel, G. S., Naitian, P. M. & Newman, R. C.) 500–507 (Electrochemical Society, Pennington, New Jersey, 2000).
- Pickering, H. W. & Wagner, C. Electrolytic dissolution of binary alloys containing a noble metal. *J. Electrochem. Soc.* **114**, 698–706 (1967).
- Sieradzki, K., Corderman, R. R., Shukla, K. & Newman, R. C. Computer simulations of corrosion: selective dissolution of binary alloys. *Phil. Mag. A* **59**, 713–746 (1989).
- Sieradzki, K. Curvature effects in alloy dissolution. *J. Electrochem. Soc.* **140**, 2868–2872 (1993).
- Wagner, C. Contribution to the theory of electropolishing. *J. Electrochem. Soc.* **101**, 225–228 (1953).
- Erlebach, J. in *Dynamics of Crystal Surfaces and Interfaces* (eds Duxbury, P. & Prentice, T.) 24–28 (Plenum, New York, 1997).
- Wagner, K., Brankovic, S. R., Dmitrov, N. & Sieradzki, K. Dealloying below the critical potential. *J. Electrochem. Soc.* **144**, 3545–3555 (1997).
- Cahn, J. W. & Hilliard, J. E. Free energy of a nonuniform system. I. Interfacial free energy. *J. Chem. Phys.* **28**, 258–267 (1958).
- Cahn, J. W. & Hilliard, J. E. Free energy of a nonuniform system. III. Nucleation in a two-component incompressible fluid. *J. Chem. Phys.* **31**, 688–699 (1959).
- Hilliard, J. E. in *Solidification* 497–560 (American Society for Metals, Metals Park, Ohio, 1971).
- Ben-Jacob, E., Goldenfeld, N., Langer, J. S. & Schon, G. Dynamics of interfacial pattern formation. *Phys. Rev. Lett.* **51**, 1930–1932 (1983).
- Mullins, W. W. Theory of thermal grooving. *J. Appl. Phys.* **28**, 333–339 (1957).
- Kessler, D. A., Koplik, J. & Levine, H. Geometrical models of interface evolution. II. Numerical simulation. *Phys. Rev. A* **30**, 3161–3174 (1984).
- Hou, T. Y., Lowengrub, J. S. & Shelley, M. J. Removing the stiffness from interfacial flow with surface tension. *J. Comp. Phys.* **114**, 312–338 (1994).
- Barabasi, A. L. & Stanley, H. E. *Fractal Concepts in Surface Growth* (Cambridge Univ. Press, 1995).
- Haasen, P. *Physical Metallurgy*, (Cambridge Univ. Press, 1986).
- Fory, A. J. in *Sir Charles Frank: An 80th Birthday Tribute* (ed. Chamber, R. G.) 164–187 (Adam Hilger, Bristol, 1991).
- Tulimieri, D. J., Yoon, J. & Chan, M. H. W. Ordering of helium mixtures in porous gold. *Phys. Rev. Lett.* **82**, 121–124 (1999).

#### Acknowledgements

This work was supported by the US Department of Energy, Basic Energy Sciences. The research of A.K. also benefited from computer time allocation at NU-ASCC. K.S. thanks the AFOSR for support.

Correspondence and requests for materials should be addressed to J.E. (e-mail: Jonh.Erlebach@jhu.edu).

## Ice shelves in the Pleistocene Arctic Ocean inferred from glaciogenic deep-sea bedforms

Leonid Polyak\*, Margo H. Edwards†, Bernard J. Coakley‡ & Martin Jakobsson§

\* Byrd Polar Research Center, Ohio State University, Columbus, Ohio 43210, USA

† Hawaii Mapping Research Group, Hawaii Institute of Geophysics and Planetology, University of Hawaii, Honolulu, Hawaii 96822, USA

‡ Department of Geology, Tulane University, New Orleans, Louisiana 70118, USA

§ Department of Geology and Geochemistry, Stockholm University, 106 91 Stockholm, Sweden

It has been proposed that during Pleistocene glaciations, an ice cap of 1 kilometre or greater thickness covered the Arctic Ocean<sup>1–3</sup>. This notion contrasts with the prevailing view that the Arctic Ocean was covered only by perennial sea ice with scattered icebergs<sup>4–6</sup>. Detailed mapping of the ocean floor is the best means to resolve this issue. Although sea-floor imagery has been used to reconstruct the glacial history of the Antarctic shelf<sup>7–9</sup>, little data have been collected in the Arctic Ocean because of operational constraints<sup>10,11</sup>. The use of a geophysical mapping system during the submarine SCICEX expedition in 1999<sup>12</sup> provided the opportunity to perform such an investigation over a large portion of the Arctic Ocean. Here we analyse backscatter images and sub-bottom profiler records obtained during this expedition from depths as great as 1 kilometre. These records show multiple bedforms indicative of glacial scouring and moulding of sea floor, combined with large-scale erosion of submarine ridge crests. These distinct glaciogenic features demonstrate that immense, Antarctic-type ice shelves up to 1 kilometre thick and hundreds of kilometres long existed in the Arctic Ocean during Pleistocene glaciations.

The central Arctic Ocean contains relatively shallow areas (water depths <1,000 m; see Fig. 1) on Yermak plateau, Lomonosov ridge and Chukchi borderland—which includes Chukchi plateau, Chukchi rise and Northwind ridge. During the SCICEX-99 expedition, conducted on the nuclear-powered submarine USS *Hawkbill*, shallow sea-floor areas were targeted for mapping to detect glaciogenic bedforms. Sea-floor images (collected using a submarine-mounted 12-kHz swath bathymetry and sidescan sonar<sup>13</sup>) from the Chukchi borderland and the Lomonosov ridge show a variety of bedforms, including random or subparallel scours, parallel lineations, and transverse ridges. On the records from the chirp sub-bottom profiler, these bedforms are associated with planed ridge crests with rough microrelief and obvious angular unconformities cut into the stratified sediments.

Randomly oriented furrows, typically <100-m wide and up to 30-m deep, densely cover the shallowest, <400-m-deep portions of sea floor on the Chukchi borderland and adjacent continental margin (Fig. 2a). Isolated larger scours up to 700-m wide and over 10-km long occur as deep as 500 m. Even greater depths, exceeding 900 m, are attained by closely spaced, subparallel scours on the Lomonosov ridge. Sea-floor scours are known to be formed by the drift of icebergs and pack-ice ridges<sup>14</sup>. At present, icebergs in the Arctic Ocean have at most 50-m draughts<sup>15</sup>, whereas icebergs off Antarctica and Greenland reach depths of 500–550 m (refs 15, 16). The largest depths of gouged sea floor, extending to 850 m, have been reported from the Yermak plateau<sup>10</sup>, matching the depth of scours on the Lomonosov ridge.

Below the depth range of dense scouring, the sea floor exhibits

† Present address: Center for Coastal Mapping, University of New Hampshire, Durham, New Hampshire 03824, USA.



**This Page is Inserted by IFW Indexing and Scanning  
Operations and is not part of the Official Record**

**BEST AVAILABLE IMAGES**

Defective images within this document are accurate representations of the original documents submitted by the applicant.

Defects in the images include but are not limited to the items checked:

- ☐ **BLACK BORDERS**
- ☐ **IMAGE CUT OFF AT TOP, BOTTOM OR SIDES**
- ☐ **FADED TEXT OR DRAWING**
- ☐ **BLURRED OR ILLEGIBLE TEXT OR DRAWING**
- ☐ **SKEWED/SLANTED IMAGES**
- ☐ **COLOR OR BLACK AND WHITE PHOTOGRAPHS**
- ☐ **GRAY SCALE DOCUMENTS**
- ☒ **LINES OR MARKS ON ORIGINAL DOCUMENT**
- ☐ **REFERENCE(S) OR EXHIBIT(S) SUBMITTED ARE POOR QUALITY**
- ☐ **OTHER:** \_\_\_\_\_

**IMAGES ARE BEST AVAILABLE COPY.**

**As rescanning these documents will not correct the image problems checked, please do not report these problems to the IFW Image Problem Mailbox.**

**THIS PAGE BLANK (USPTO)**